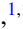# Photonic Chern insulators made of gyromagnetic hyperbolic metamaterials

Ruei-Cheng Shiu,[1] Hsun-Chi Chan,[1] Hai-Xiao Wang ©,[1,2,3] and Guang-Yu Guo[1,2,*]

[1]*Department of Physics and Center for Theoretical Physics, National Taiwan University, Taipei 10617, Taiwan*
[2]*Physics Division, National Center for Theoretical Sciences, Hsinchu 30013, Taiwan*
[3]*School of Physical Science and Technology, Guangxi Normal University, Guilin 54001, People's Republic of China*

Controlling light propagation using artificial photonic crystals and electromagnetic metamaterials is an important topic in the vibrant field of photonics. Notably, chiral edge states on the surface or at the interface of photonic Chern insulators can be used to make reflection-free waveguides. Here, by both theoretical analysis and electromagnetic simulations, we demonstrate that gyromagnetic hyperbolic metamaterials (GHM) are photonic Chern insulators with superior properties. As a novel mechanism, the simultaneous occurrence of the hyperbolic and gyromagnetic effects in these metamaterials is shown to open the large topological band gaps with a gap Chern number of one. Importantly, the GHM Chern insulators possess nonradiative chiral edge modes on their surfaces, and thus allow us to fabricate unidirectional waveguides without cladding metals which generally incur considerable Ohmic loss. Furthermore, the photonic edge states in the proposed Chern insulators are robust against disorder on a wide range of length scales, in strong contrast to crystalline topological insulators, and the light flow direction on the surface of the Chern insulators can be easily flipped by switching the direction of an applied magnetic field. Fascinatingly, we find that negative refraction of the topological surface wave occurs at the boundary between the GHMs with the opposite signs of gyromagnetic parameters. Finally, we show that compared with other photonic topological materials such as chiral hyperbolic materials, the present GHM Chern insulators can be much easier to fabricate.

I. INTRODUCTION

Control over the propagation of light using artificial photonic crystals [1,2] and electromagnetic metamaterials [3] has received enormous attention in recent decades mainly because of its importance for many applications in the vibrant field of photonics. For example, metamaterials such as left-handed media [4,5] have shown promising potential for novel technologies [6,7]. In recent decades, great progress in this field has been often made by taking advantages of analogies with electronic systems in solid state physics. For example, the concept of a photonic band gap material [1,2], a man-made system with a periodic dielectric function, was inspired by the electronic Bloch states in a crystalline semiconductor.

More recently, there have been growing interests in using topological photonic materials [8] to manipulate the flow of light, again inspired by the recent developments of electronic topological materials [9–11]. In particular, the electronic quantum anomalous Hall (QAH) phase is a two-dimensional (2D) bulk ferromagnetic insulator with a nonzero Chern number in the presence of spin-orbit coupling (SOC) but in the absence of applied magnetic fields [12,13]. The associated metallic chiral edge states in this Chern insulator carry dissipationless unidirectional electric current. Haldane and Raghu recently proposed [14] to construct analogs of this intriguing QAH phase in photonic crystals made of time-reversal symmetry (TRS) breaking materials to realize unidi-

rectional optical waveguides. Subsequently, these topological electromagnetic states in a number of gyromagnetic photonic crystals with broken TRS were further proposed [15–21] and observed [22–25]. Interestingly, a photonic analog of electronic quantum spin Hall effect in 2D topological insulators with TRS [9,10] were also observed in bianisotropic photonic crystals [26–28].

Nevertheless, investigations of photonic unidirectional edge modes have mostly been limited to topological photonic crystals periodic on the scale of the operational wavelength, and this considerably restricts the applications of topological photonic materials. Very recently, Gao *et al.* [29] demonstrated a theoretically topological photonic phase in chiral hyperbolic metamaterials (CHM) made of continuous TRS media with photonic edge states robust against disorder on all length scales [29]. In hyperbolic metamaterials [30], which are plasmonic metamaterials, equifrequency surfaces (EFSs) of transverse electric-field (TE) and transverse magnetic-field (TM) modes are degenerate on the high-symmetry points in the momentum space [see Fig. 1(b)]. When the bianisotropic property (chirality) is introduced in hyperbolic metamaterials with TRS, which then become CHMs, the degeneracies are broken due to the coupling between TE and TM modes [26] and consequently, a nontrivial band gap is opened [29]. The nontrivial topology of the CHM results from the nonzero Berry curvature due to the chirality (equivalent to the SOC in electronic topological insulators) and broken spatial inversion symmetry in continuous medium [31].

In this work, as a novel mechanism for controlling light flow, we introduce the photonic Chern insulators made of
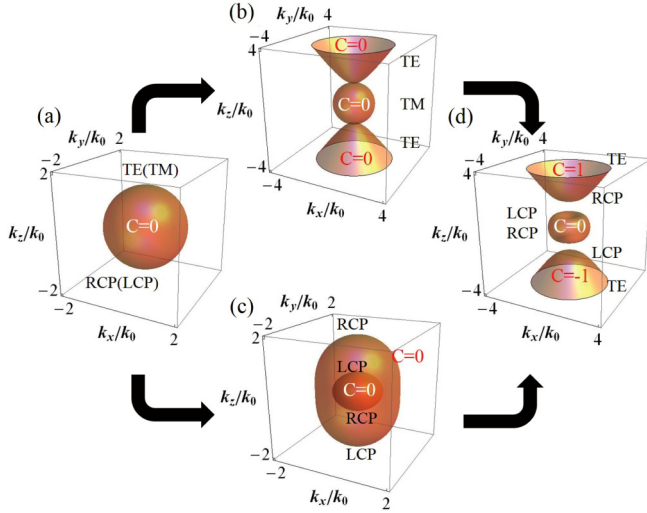
---

*gyguo@phys.ntu.edu.tw

FIG. 1. EFS evolution from (a) an isotropic medium ($\epsilon_{xx} = \epsilon_{zz} = 2$ and $\gamma = 0$) to (d) a GHM ($\epsilon_{xx} = 2$, $\epsilon_{zz} = -1$, and $\gamma = 0.8$) via either (b) a hyperbolic metamaterial ($\epsilon_{xx} = 2$, $\epsilon_{zz} = -1$, and $\gamma = 0$) or (c) a gyromagnetic medium ($\epsilon_{xx} = \epsilon_{zz} = 2$ and $\gamma = 0.8$). TE (TM) and RCP (LCP) denote TE (TM) polarization and right-handed (left-handed) circular polarization, respectively.

continuous gyromagnetic hyperbolic metamaterials (GHM) with the band gap opened by the TRS-breaking gyromagnetic effect [Figs. 1(b) and 1(c)]. The nontrivial topology is demonstrated by the calculated Berry curvature and nonzero Chern number due to the broken TRS. The unidirectional backscattering-immune nonradiative edge modes at the interface between the GHM and vacuum are uncovered by the finite-element electromagnetic simulations. As in the photonic quantum spin Hall insulators (QSHI) made of the CHMs [29], the photonic edge states in our Chern insulators are robust against disorder on all length scales. In contrast to the QSHIs [29], however, the light flow direction on the surface of our Chern insulators can be easily flipped by switching the direction of applied magnetic fields. Furthermore, our Chern insulators made of the GHM can be easily fabricated.

II. GYROMAGNETIC HYPERBOLIC METAMATERIAL

We consider a GHM as a hyperbolic metamaterial [30] with the gyromagnetic response which is described by the constitutive relation

$$\begin{pmatrix} \mathbf{D} \\ \mathbf{B} \end{pmatrix} = \begin{pmatrix} \varepsilon_0 \hat{\epsilon}_r & 0 \\ 0 & \mu_0 \hat{\mu}_r \end{pmatrix} \begin{pmatrix} \mathbf{E} \\ \mathbf{H} \end{pmatrix}, \tag{1}$$

where

$$\hat{\epsilon}_r = \begin{pmatrix} \epsilon_{xx} & 0 & 0 \\ 0 & \epsilon_{yy} & 0 \\ 0 & 0 & \epsilon_{zz} \end{pmatrix}, \quad \hat{\mu}_r = \begin{pmatrix} \mu_{xx} & -i\gamma & 0 \\ i\gamma & \mu_{yy} & 0 \\ 0 & 0 & \mu_{zz} \end{pmatrix} \tag{2}$$

are the relative permittivity and permeability tensors, respectively, and γ is the gyromagnetic parameter, representing the degree of TRS breaking upon application of a magnetic field in the z direction (gyromagnetic effect). For simplicity, let us set $\mu_{xx} = \mu_{yy} = \mu_{zz} = 1$ and $\epsilon_{xx} = \epsilon_{yy}$ such that EFS dispersions are isotropic in the xy plane. Note that small loss

would not affect the topology of such an effective medium system (see Ref. [32] and references therein). As a result, the surface states still match the lossless analytical solution [33,34] and can be detected. This is also demonstrated in Appendix A below. The propagation behavior of the gyromagnetic hyperbolic metamaterials can be described by the wave equation of the electric field $\mathbf{E} = (E_x, E_y, E_z)^T$ as

$$\mathbf{k} \times \hat{\mu}_r^{-1} \mathbf{k} \times \mathbf{E} + k_0^2 \hat{\epsilon}_r \mathbf{E} = 0, \tag{3}$$

where $\mathbf{k} = (k_x, k_x, k_z)$ is the wave vector, and $k_0 = \omega/c$ is the wave number in vacuum. Equation (3) can be rewritten in the matrix form as

$$\begin{pmatrix} \alpha k_0^2 - \frac{k_y^2}{\mu} - A k_z^2 & \frac{k_x k_y}{\mu} + B k_z^2 & A k_x k_z - B k_y k_z \\ \frac{k_x k_y}{\mu} - B k_z^2 & \alpha k_0^2 - \frac{k_x^2}{\mu} - A k_z^2 & A k_y k_z + B k_x k_z \\ A k_x k_z + B k_y k_z & A k_y k_z - B k_x k_z & \beta k_0^2 - A k_t^2 \end{pmatrix} \begin{pmatrix} E_x \\ E_y \\ E_z \end{pmatrix}$$
$$= 0, \tag{4}$$

where $k_x^2 + k_y^2 = k_t^2$, $A = \frac{\mu}{\mu^2 - \gamma^2}$, $B = \frac{\gamma}{\mu^2 - \gamma^2}$. The nontrivial solutions of $\mathbf{E} = (E_x, E_y, E_z)^T$ exist when the determinant of the matrix on the left side of Eq. (4) equals zero, resulting in the eigenequation of

$$\alpha^2 \beta k_0^4 \mu - \alpha k_0^2 \left[k_t^2 (\alpha A \mu + \beta) \right.$$
$$\left. + 2 \beta A \mu k_z^2 \right] + A (k_t^2 + k_z^2)(\alpha k_t^2 + \beta k_z^2)$$
$$= 0. \tag{5}$$

Starting with an isotropic optical medium with $\epsilon_{xx} = \epsilon_{zz} = 2$ and $\gamma = 0$, one has two routes to arrive at a GHM, as illustrated in Fig. 1. The EFS dispersion of the isotropic medium is a perfect sphere, as shown in Fig. 1(a). Furthermore, the eigenstates consisting of transverse electric mode (TE) ($E_x = E_y = 0$, $H_z \neq 0$) and transverse magnetic modes (TM) ($H_x = H_y = 0$, $E_z \neq 0$), are degenerate and their dispersions are identical and on the same sphere. When the isotropic medium is transformed to a hyperbolic metamaterial ($\epsilon_{xx} = 2$, $\epsilon_{zz} = -1$, and $\gamma = 0$) by varying ϵ_{zz} from 2 to -1, the EFS sphere of the TE mode splits and becomes two parabola along the k_z axis while that of the TM mode remains spherical, as depicted in Fig. 1(b) [see Figs. 2(a) and 2(b) for polarization analysis]. This is because TM "sees" $\epsilon_{xx} = \epsilon_{yy} = 2$ only while, in contrast, TE sees $\epsilon_{xx} = \epsilon_{yy} = 2$ and $\epsilon_{zz} = -1$. Interestingly, the two TM parabola touch the TE sphere at $k_z = \pm 1.0 k_0$, respectively. When the gyromagnetic effect is further introduced into the system by making γ nonzero (e.g., $\gamma = 0.8$), the system becomes a GHM. As a result, a band gap is opened at both degenerate points $k_z = \pm 1.0 k_0$ [see Fig. 1(d)]. Interestingly, since the gyromagnetic effect breaks TRS, the eigenstates near $\pm 1.0 k_0$ become circularly (elliptically) polarized, while eigenstates on the upper and lower hyperbolic bands far away from the singular points remain TE polarized [see Figs. 2(c) and 2(d)].

Alternatively, one can go from an isotropic medium first to a gyromagnetic medium (e.g., $\epsilon_{xx} = \epsilon_{zz} = 2$ and $\gamma = 0.8$) [see Fig. 1(c)] and then to the GHM. In a gyromagnetic medium, because of broken TRS, TE and TM modes are coupled, resulting in the separation of the degenerate EFS spheres into two ellipsoids [Fig. 1(c)]. Also eigenstates become elliptically polarized [see Figs. 2(e) and 2(f)]. In particular, the
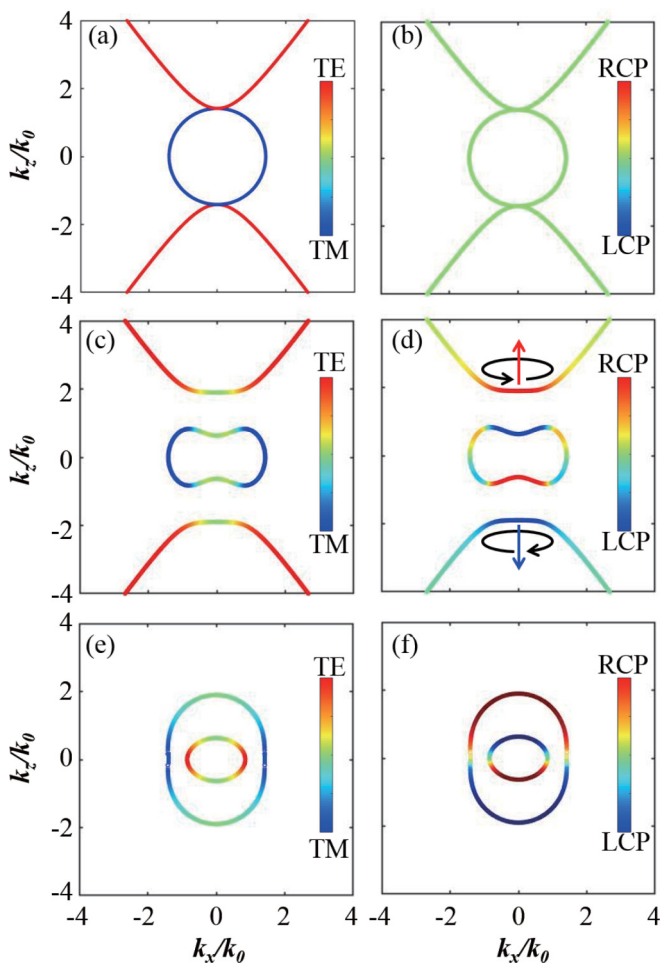
FIG. 2. Polarization analysis of eigenstates. Calculated polarization of EFS dispersion for (a) and (b) the hyperbolic metamaterial, (c) and (d) the GHM, and (e) and (f) the gyromagnetic medium. RCP (LCP) and TE (TM) denote right-handed (left-handed) circular polarization and TE (TM) polarization, respectively.

eigenstates on the top and bottom surfaces of the ellipsoids become nearly fully circularly polarized, while those in the vicinity of the $k_z = 0$ plane remain almost purely either (inner ellipsoid) TE or (outer ellipsoid) TM polarization. Throughout this paper we describe the polarizations of the eigenstates on an EFS according to the Stoke parameters [35], where the right circularly polarization (RCP) and left circularly polarization (LCP) refer to the electric field vector rotate in a right-hand and left-hand sense with respect to the direction of propagation, respectively. Finally, when ϵ_{zz} is tuned to a negative value (e.g., $\epsilon_{zz} = -1$), the system becomes a GHM and the outer ellipsoid splits to form two open parabolas, as shown in Fig. 1(d).

III. TOPOLOGICAL PHASE TRANSITION

To investigate the topological property of the EFS dispersions of all four kinds of optical media and metamaterials and also to examine the topological nature of the band gaps near $k_z = \pm k_0$, we calculate the Berry phase Φ and hence also the Chern number $\mathcal{C} = \frac{1}{2\pi}\Phi$ of all EFS surfaces [21,36].
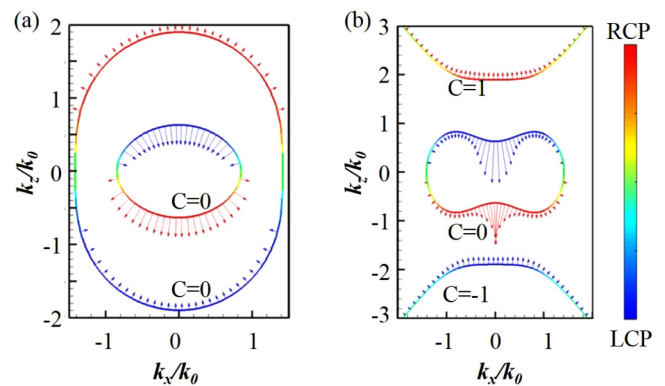

FIG. 3. Berry curvature distribution on the EFSs of the gyromagnetic hyperbolic metamaterials with (a) $\epsilon_{xx} = \epsilon_{zz} = 2$ and $\gamma = 0.8$ as well as (b) $\epsilon_{xx} = 2$, $\epsilon_{zz} = -1$, and $\gamma = 1.2$. The calculated Chern number (C) for each EFS is also given.

The Berry phase of an EFS is given by a surface integral over its whole surface $\Phi = \iint \mathbf{F}(\mathbf{k}) \cdot d\mathbf{s}$ where the Berry curvature $\mathbf{F}(\mathbf{k}) = \nabla \times \langle\psi(\mathbf{k})|i\nabla|\psi(\mathbf{k})\rangle$, $d\mathbf{s}$ is the surface element vector, and $\psi(\mathbf{k})$ is the eigenstate of Eq. (4). Following our previous work [21], we adopt the efficient numerical algorithm reported in Ref. [36] to evaluate the Berry curvature $\mathbf{F}(\mathbf{k})$. That is, we divide an EFS into a large number (N) of small quadrilateral surface elements. For element i, the Berry phase $\Delta\Phi_i$ is given by the eigenstates at the four corner $\mathbf{k}$ points ($\mathbf{k}_{00}$, $\mathbf{k}_{01}$, $\mathbf{k}_{10}$, $\mathbf{k}_{11}$) of the element, i.e.,

$$\Delta\Phi_i = \frac{1}{i}\ln\frac{\langle\psi(\mathbf{k}_{00})|\psi(\mathbf{k}_{10})\rangle\langle\psi(\mathbf{k}_{10})|\psi(\mathbf{k}_{11})\rangle}{\langle\psi(\mathbf{k}_{00})|\psi(\mathbf{k}_{01})\rangle\langle\psi(\mathbf{k}_{01})|\psi(\mathbf{k}_{11})\rangle}. \quad (6)$$

Therefore, the Berry phase of the EFS is given by $\Phi = \sum_{i=1}^{N}\Delta\Phi_i$. Note that, in principle, the Berry phase and the Chern number are well defined only for a closed surface. Fortunately, our test calculations show that the Berry curvature $\mathbf{F}(\mathbf{k})$ is negligibly small when the radial wave vector $k_\rho = \sqrt{k_x^2 + k_y^2} > 15$. Therefore, although the hyperbolic shaped EFS surfaces are open (Figs. 1 and 2), we find that the calculated Chern numbers would converge well to integers as long as the surface integration is carried out from the k_0 up to the radial wave vector $k_\rho = \sqrt{k_x^2 + k_y^2}$ being larger than 15. The Chern numbers calculated in this way are shown in Fig. 1, and the Berry curvature distributions are displayed in Fig. 3. We notice that the Berry curvature has the following symmetry properties: (a) $\mathbf{F}(\mathbf{k}) = \mathbf{F}(-\mathbf{k})$ if the system has the spatial inversion symmetry (IS) and (b) $\mathbf{F}(\mathbf{k}) = -\mathbf{F}(-\mathbf{k})$ if the system has the TRS symmetry. Therefore, the Berry curvature is identically zero and hence the Chern number is zero for both isotropic medium and hyperbolic metamaterial because they have both IS and TRS [see Figs. 1(a) and 1(b)].

In contrast, the Berry curvatures become nonzero in both gyromagnetic medium and GHM since their TRS is broken, as shown in Fig. 3. Nevertheless, in the gyromagnetic medium, the Berry curvatures on each EFS ellipsoid form an odd function of k_z [see Fig. 3(a)] because of the presence of the IS symmetry. Consequently, the sum of the Berry curvatures on the EFS surface of each ellipsoid (i.e., the Berry phase and the Chern number) remains zero [Fig. 1(c)].

This is also true for the inner ellipsoid in the GHM [Fig. 3(b)] and hence the Chern number of the inner EFS is zero [Fig. 1(d)]. However, the outer ellipsoid in the GHM now splits and hence transforms into two open parabolic surfaces with Berry curvatures pointing to the positive z direction. Consequently, the upper and lower open surfaces each acquires a Chern number of $+1$ and -1, respectively. Therefore, the phase transformation from the hyperbolic to gyromagnetic hyperbolic due to the gyromagnetic effect is a topological one, and the band gaps centered at $\pm k_0$ are topologically nontrivial.

IV. NONRADIATIVE ONE-WAY PHOTONIC EDGE MODE

According to the bulk-edge correspondence, the gap Chern number of $\Delta C = -1$ implies that there is one propagating edge mode in each band gap for each air-GHM interface.

Furthermore, these edge modes are chiral and topology protected, i.e., they are reflection-free one-way edge states. To verify these amazing predictions, we first follow the method proposed in Ref. [37] to calculate analytically the surface bands between the air and GHM material. Let us consider the interface between air ($y > 0$) and GHM ($y < 0$) on the xz plane ($y = 0$) [see Fig. 4(a)]. The effect of the finite size of the CHM on the topological edge states have been recently discussed in Ref. [38]. Here we also examine the finite size effect on the edge modes of the GHM in Appendix B. As a result, in this work we assume that the thickness (d) of the GHM along the y direction is larger than the wavelength (λ) so that there would be negligible interaction between the edge modes on the top and bottom surfaces of the GHM slab. The wave vector in the GHM normal to the interface can be obtained by solving Eq. (5):

$$k_y^{\text{GHM}} = \pm \left(\frac{\alpha k_0^2[\alpha\mu^2 + \beta(\mu^2 - \gamma^2)] - 2\alpha\mu k_x^2 - \alpha\mu k_z^2 - \beta\mu k_z^2 \pm Y}{2\alpha\mu} \right)^{1/2}, \tag{7}$$

where

$$Y \equiv \sqrt{\alpha^2 k_0^4[\alpha\mu^2 + \beta(\gamma^2 - \mu^2)]^2 + 2\alpha k_0^2\mu k_z^2[-\alpha^2\mu^2 + \alpha\beta(\gamma^2 + 2\mu^2) + \beta^2(\gamma^2 - \mu^2)] + \mu^2(\alpha - \beta)^2 k_z^4}. \tag{8}$$

Then the two linear independent eigenfields in the GHM, $\mathbf{E}_i(k_x, k_y, k_z)$ ($i = 3, 4$), can be obtained by solving the null space of Eq. (4) with $k_y = k_y(k_x, k_z)$ from Eq. (4). Note that we need to choose two out of four roots of k_y in Eq. (4) such that $\text{Im}(k_y)$ would be smaller than zero due to the assumption of the decay wave normal to the interface. Once $\mathbf{E}_i$ are obtained, $\mathbf{H}_i$ can also be obtained via Faraday's law $\mathbf{H}_i = \frac{1}{Z_0}\mathbf{k} \times \mathbf{E}_i$. Similarly, two orthogonal eigenfields in the air can be expressed as

$$\mathbf{E}_1 = \begin{pmatrix} -k_z \\ 0 \\ k_x \end{pmatrix}, \quad \mathbf{E}_2 = \begin{pmatrix} -k_y \\ k_x \\ 0 \end{pmatrix}, \quad \mathbf{H}_1 = \frac{1}{Z_0}\begin{pmatrix} k_x k_y \\ -k_x^2 - k_z^2 \\ k_y k_z \end{pmatrix}, \quad \mathbf{H}_2 = \frac{1}{Z_0}\begin{pmatrix} -k_x k_z \\ -k_y k_z \\ k_x^2 + k_y^2 \end{pmatrix}, \tag{9}$$

where $Z_0 = \sqrt{\mu_0/\epsilon_0}$ is the vacuum impedance, and $k_y = i\sqrt{k_x^2 + k_z^2 - k_0^2}$. Since the tangential components of the electromagnetic fields should be continuous across the interface, we arrive at $\text{Det}(D) = 0$ with

$$D(k_x, k_z) = \begin{pmatrix} -k_z & -k_y & E_{3x} & E_{4x} \\ k_x & 0 & E_{3z} & E_{4z} \\ k_x k_y & -k_x k_z & H_{3x} & H_{4x} \\ k_y k_z & k_x^2 + k_y^2 & H_{3z} & H_{4z} \end{pmatrix}. \tag{10}$$

One can then obtain the surface mode, of which the fields in air and GHM must decay exponentially along the vertical direction of the interface, by solving $\det(D) = 0$. To do this, it is important to choose the range of the imaginary part of k_y (k_y^{GHM}) in the vacuum (GHM) to be positive (negative). In other words, the fields in the air and GHM must decay exponentially along the vertical direction of the interface. The obtained dispersions of the surface modes are displayed in Fig. 4(b) (blue and red lines), together the bulk bands (black curves). Figure 4(b) shows that within the bulk band gaps, there is indeed one edge state for both top (red curve) and bottom (blue curve) interfaces between air and the GHM slab in each bulk band gap. It should be noted that the chiral edge states have mirror symmetry with respect to the

$k_z = 0$ plane, i.e., the chiralities of the edge states above and below the $k_z = 0$ plane, are different, in contrast to that in the CHM [29].

To demonstrate the unidirectional nature of the edge states, we further simulate light propagation in the air-GHM interface by putting a line source along the z axis at $x = 0$. The results are displayed in Figs. 4(c)–4(f). Our simulations show clearly that light on each interface runs without attenuation in either $+x$ or $-x$ direction but not both directions, i.e., light propagation on the edges is unidirectional. Surprisingly, Fig. 4(c) [Fig. 4(d)] shows that both edge modes of $k_z = \pm 1.6k_0$ carry light towards $-x$ [$+x$] direction. Intuitively, light beams with opposite signs of k_z would propagate along the oppositive directions of the x axis. This counterintuitive phenomenon results from the fact that the chiralities of the edge modes above and below the $k_z = 0$ plane are opposite, as mentioned in the proceeding paragraph. Moreover, Figs. 4(c) and 4(d) show that the direction of light propagation depends on the sign of gyromagnetic parameter γ, demonstrating that one can control light transmission direction by switching the magnetization direction of the GHM slab. It is also evident from Figs. 4(d) and 4(e) that the light propagates along the opposite directions at top and bottom surface. Figure 4(f) shows that the light beam can also overcome the obstacles on
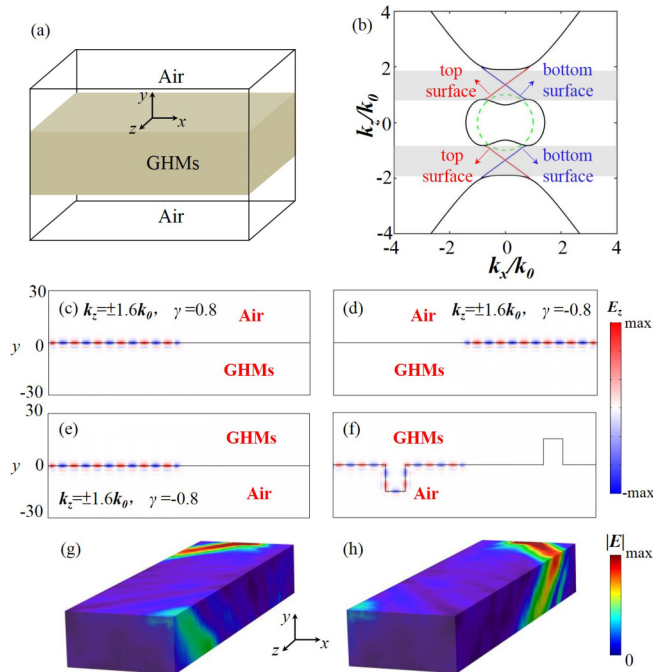
FIG. 4. One-way propagating edge states. (a) A GHM slab in air. (b) Calculated EFS dispersions for the GHM slab in air (a). Black, red, and blue lines denote dispersions of bulk state, top, and bottom edge states, respectively. The dashed green circle denotes light cone. (c) and (d) Simulated propagations of light emitted by a line source at $x = 0$ on the top surface at $k_z = \pm 1.6k_0$ with $\gamma = 0.8$ and $\gamma = -0.8$, respectively. (e) The same as in (d) but on the bottom surface. (f) The same as in (c) except that the surface is now uneven, which does not stop light from propagating along the negative x direction. (g) and (h) 3D stimulated propagation of the chiral edge mode on the surface of a lossy cuboid-shaped GHM with (g) $\gamma = 0.8 + 0.01i$ and (h) $\gamma = -0.8 - 0.01i$, emitted by a radiation source at $k_z = 1.6k_0$. Note that here the wave propagates along the z direction with the decreasing amplitude because of the small added loss (see Appendix B for more discussion on the effect of the dissipation loss).
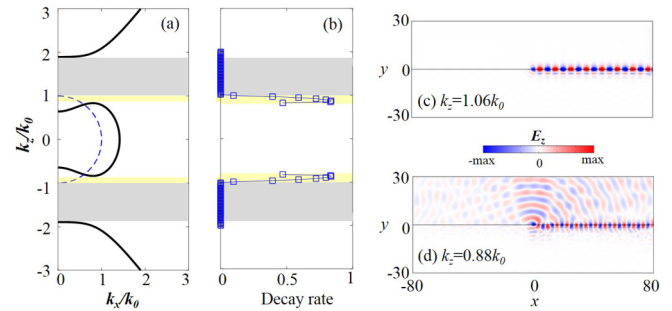

FIG. 5. (a) EFS dispersions and (b) decay rate of the electromagnetic waves for the GHM slab in the air. In (a), the solid black and dashed blue curves denote the dispersions of the bulk states and the air, respectively. In (a) and (b), the yellow regions denote the overlap regions of the air dispersion and bulk gap regions, while the gray regions denote the complete gap regions. (c) and (d) Electric field distributions of the edge states with (c) $k_z = 1.06k_0$ and (d) $k_z = 0.88k_0$, respectively. Note that in (c), the electric field is completely confined to the edge of the GHM slab and hence there is no radiative energy loss, because the k_z is outside the light EFS sphere. In contrast, in (d), because the k_z is within the light EFS sphere, the electromagnetic wave of the edge state propagates strongly into the air, resulting in a large radiative energy loss.

the surface, indicating light propagation is reflection-free due to the topological protection. Finally, we have also performed the 3D simulations for the cuboid-shaped GHMs with a small loss surrounded by air. The results are displayed in Figs. 4(g) and 4(h) for gyromagnetic parameters of $\pm \gamma$. We consider the loss by taking the gyromagnetic parameter as a complex number with a small imaginary part. A small port is positioned at the interface as the radiation source. Both Figs. 4(g) and 4(h) show the backscattering immune transportation of the edge states bending around the z-invariant sharp corners, thereby demonstrating the robustness of the one-way edge states.

Finally, let us discuss the nonradiative property [39,40] of the edge states of the GHM. A GHM is based on a hyperbolic metamaterial, which is generally a bilayer superlattice consisting of a metal layer and a dielectric layer stacked along the normal direction (see the next section for details). Thus, the GHMs possess the property of surface plasmon polaritons (SPPs). Compared with the electromagnetic waves in the air,

the SPPs are slower waves and hence have larger wave vectors than that of light in the air. As a result, the edge states on a GHM may inherit this larger wave vector propagation, as shown in Fig. 4(b). Therefore, there may be no intersection between the air light line and edge states, i.e., the edge states are out of the light line. Consequently, the edge state would propagate on the interface without radiation [Fig. 5(c)] because the edge states cannot couple to the electromagnetic waves in the air. In strong contrast, most of photonic topological insulators are made of photonic crystals and consequently, the one way edge states on the interfaces of these insulators suffer from severe radiation loss and a metal wall serving as a cladding perfect electric conductor or a perfect magnetic conductor has to be added to the surrounding edges to stop radiation loss into the air [15,22,23]. In practice, there is no lossless perfect conductor and even good metals such as copper used as the cladding walls absorb the radiation significantly. This certainly hinders their applications. In contrast, in a GHM, the air serves as the good insulator for stopping the radiation of the edge states into the air [Fig. 5(c)]. To further understand this intriguing property, let us divide the k_z range in Fig. 5(a) into two regions. The yellow region refers to the k_z region that supports both edge state and air mode, while the gray region refers to the k_z region that supports the edge state only. To characterize the nonradiative property of the edge state, we introduce the radiative decay rate as the ratio of the radiation power harvested in the air to the radiation power of the source [41]. As shown in Fig. 5(b), the decay rate is zero in the gray region, indicating that the edge state propagates without radiating into the air [see Fig. 5(c) for $k_z = 1.06k_0$]. In other words, here the air serves as a good insulator for the edge states of the GHM. In contrast, the decay rate grows sharply to 1.0 as k_z enters the yellow region because the edge states now couple to the wave in the air [see Fig. 5(d) with $k_z = 0.88k_0$].
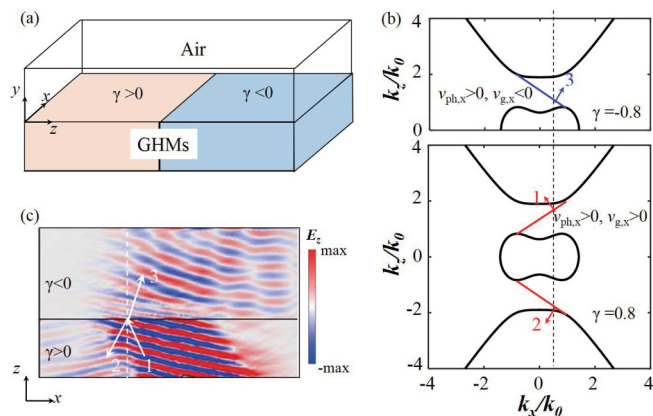
FIG. 6. Negative refraction of the topological surface states at the interface between two different GHMs. (a) Schematic of the GHM system consisting of a slab made of two GHMs with negative and positive gyromagnetic ratio. (b) Illustration of the negative refraction through an EFS analysis, where $v_{g,x}$ and $v_{ph,x}$ denote the x components of the group and phase velocities, respectively. (c) Stimulated negative refraction, where the incident, reflected, and transmitted waves at the interface between the two different GHMs are denoted as 1, 2, and 3, respectively.

V. NEGATIVE REFRACTION OF EDGE MODE

Another interesting property of the topological surface states of the GHM is negative refraction, similar to that of the CHM reported recently in Ref. [38]. Specifically, let us consider a slab consisting of two GHMs with positive and negative gyromagnetic ratio, respectively [see Fig. 6(a)]. Clearly the two interfaces between the two GHMs and air would support edge states with opposite chiralities, as discussed in the proceeding section. As shown in Fig. 6(b), the x component of the group velocity (energy flow) of all the surface states of the GHM with $\gamma = -0.8$ (the blue line in the upper panel) is positive ($v_{g,x} > 0$), while the phase velocity ($v_{ph,x} = \omega/k_x$) changes sign across $k_z = 0$. As a result, in the $k_x < 0$ region the x components of the group velocity and phase velocity have opposite signs ($v_{g,x} > 0$ and $v_{ph,x} < 0$) [see Fig. 4(b)]. This is the signature of negative refraction [38]. On the contrary, the surface states on the GHM with $\gamma = 0.8$ in the $k_x < 0$ region have $v_{g,x} < 0$ and $v_{ph,x} < 0$ [see lower panel of Fig. 6(b)]. According to the principle of conservation of the momentum parallel to the interface [42], the group velocities of the three points intersecting the surface modes will give the propagation directions of the surface waves [Fig. 6(b)]. Consequently, as shown in Fig. 6(c), the incident (wave 1) and refracted (wave 3) surface waves lie on the same side of the normal line, indicating a negative refraction.

To verify this interesting finding, we perform a numerical simulation in which a surface wave with $k_x = 0.25k_0$ is excited. The result, displayed in Fig. 6(c), indeed shows that the incident (wave 1) and refracted (wave 3) edge modes lie on the same side of the normal line, thus indicating negative refraction. The existence of negative refraction of the topological surface states would lead to many interesting effects [4–6,42–46] such as superlens effect [6,43–45] and suppression of reflected waves [42].
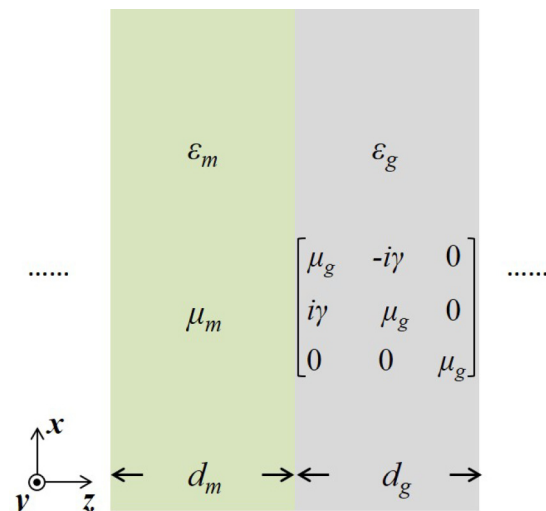

FIG. 7. Proposed gyromagnetic hyperbolic metamaterial as a bilayer superlattice composed of a gyromagnetic slab and a metal slab.

VI. REALIZATION OF THE PROPOSED GYROMAGNETIC HYPERBOLIC METAMATERIALS

The hyperbolic metamaterials are a highly anisotropic material with real parts of the principal components of its permittivity tensor having opposite signs [30] and have been intensively investigated because of this unique property. Here we consider a bilayer superlattice composed of a metal layer with relative permittivity ϵ_m and thickness d_m and a dielectric layer with relative permittivity ϵ_d and thickness d_d stacked along the z direction [47]. The effective dielectric constant of this metamaterial is given by

$$\epsilon_{\text{eff}} = \begin{bmatrix} \epsilon_{xx} & 0 & 0 \\ 0 & \epsilon_{yy} & 0 \\ 0 & 0 & \epsilon_{zz} \end{bmatrix}, \tag{11}$$

where

$$\epsilon_{xx} = \epsilon_{yy} = \frac{\epsilon_m d_m + \epsilon_d d_d}{d_m + d_d}, \tag{12a}$$

$$\frac{1}{\epsilon_{zz}} = \frac{d_m/\epsilon_m + d_d/\epsilon_d}{d_m + d_d}. \tag{12b}$$

If the dielectric layer is replaced by a gyromagnetic medium layer, the superlattice becomes a gyromagnetic hyperbolic metamaterial with its relative permeability tensors $\begin{bmatrix} \mu_g & -i\gamma & 0 \\ i\gamma & \mu_g & 0 \\ 0 & 0 & \mu_g \end{bmatrix}$ and $\begin{bmatrix} 1 & 0 & 0 \\ 0 & 1 & 0 \\ 0 & 0 & 1 \end{bmatrix}$ for the gyromagnetic and metal layers, respectively. The bilayer superlattice with relative permittivity $\epsilon_g = \epsilon_d$ and thickness $d_g = d_d$ for the gyromagnetic layer, is schematically shown in Fig. 7.

For simplicity, let us write the fields in the metal as $(\mathbf{E}^m, \mathbf{H}^m) = (E_x^m, E_y^m, E_z^m, H_x^m, H_y^m, H_z^m)$ and in the gyromagnetic medium as $(\mathbf{E}^g, \mathbf{H}^g) = (E_x^g, E_y^g, E_z^g, H_x^g, H_y^g, H_z^g)$. We assume that the wavelength is much larger than the thickness. Using the boundary conditions that D_z, E_x, E_y, B_z, H_x, and H_y must be continuous across an interface, we obtain $\epsilon_m E_z^m = \epsilon_g E_z^g$, $E_x^m = E_x^g = E_x$, $E_y^m = E_y^g = E_y$, $H_z^m = \mu_g H_z^g$,

$H_x^m = H_x^g = H_x$, $H_y^m = H_y^g = H_y$. Consequently, the average D field and B field are

$$D_x^{\text{eff}} = \frac{d_g \epsilon_g + d_m \epsilon_m}{d_g + d_m} E_x, \quad (13a)$$

$$D_y^{\text{eff}} = \frac{d_g \epsilon_g + d_m \epsilon_m}{d_g + d_m} E_y, \quad (13b)$$

$$D_z^{\text{eff}} = \epsilon_m E_z^m = \epsilon_g E_z^m, \quad (13c)$$

$$B_x^{\text{eff}} = \frac{d_g \mu_g + d_m}{d_g + d_m} H_x - \frac{i d_g \gamma}{d_g + d_m} H_y, \quad (13d)$$

$$B_y^{\text{eff}} = \frac{d_g \mu_g + d_m}{d_g + d_m} H_y + \frac{i d_g \gamma}{d_g + d_m} H_x, \quad (13e)$$

$$B_z^{\text{eff}} = \mu_0 H_z^m = \mu_g H_z^m. \quad (13f)$$

Therefore, the effective relative permittivity and permeability tensors are given by

$$\epsilon_{\text{eff}} = \begin{bmatrix} \frac{d_g \epsilon_g + d_m \epsilon_m}{d_g + d_m} & 0 & 0 \\ 0 & \frac{d_g \epsilon_g + d_m \epsilon_m}{d_g + d_m} & 0 \\ 0 & 0 & \frac{(d_g + d_m) \epsilon_g \epsilon_m}{d_g \epsilon_m + d_m \epsilon_g} \end{bmatrix}, \quad (14a)$$

$$\mu_{\text{eff}} = \begin{bmatrix} \frac{d_g \mu_g + d_m}{d_g + d_m} & \frac{-i d_g \gamma}{d_g + d_m} & 0 \\ \frac{i d_g \gamma}{d_g + d_m} & \frac{d_g \mu_g + d_m}{d_g + d_m} & 0 \\ 0 & 0 & \frac{(d_g + d_m) \mu_g}{d_g \epsilon_m + d_m \mu_g} \end{bmatrix}. \quad (14b)$$

We can easily find suitable materials as the gyromagnetic medium and the metal slab to construct a GHM described above. For example, yttrium iron garnet (YIG) under an applied magnetic field of 1600 G has the effective relative permittivity $\epsilon_g = 15$ and permeability $\mu_g = 1.12$ and $\gamma = 0.124$ at 1.94 THz [15], and thus can be used as the gyromagnetic medium. InSb has the effective relative permittivity $\epsilon_m = -10.78$ at 1.94 THz [48] and thus can serve as the metal slab. In the bilayer multilayer, the thicknesses of the gyromagnetic medium and metal layers are taken to be the same and much less than 1.546×10^{-4} m (wavelength of 1.94 THz). In this case, the effective relative permittivity and permeability tensors can be written as

$$\epsilon_{\text{eff}} = \begin{bmatrix} 2.11 & 0 & 0 \\ 0 & 2.11 & 0 \\ 0 & 0 & -76.73 \end{bmatrix}, \quad (15a)$$

$$\mu_{\text{eff}} = \begin{bmatrix} 1.06 & 0.062i & 0 \\ -0.062i & 1.06 & 0 \\ 0 & 0 & 1.06 \end{bmatrix}. \quad (15b)$$

The EFS dispersions obtained using the effective parameters are displayed in Fig. 8. Clearly the shape of the EFS dispersions is similar to that of the EFS presented in the last section, and furthermore, the topological properties such as the Chern numbers of the bands and the topological nature of the band gaps are identical to those shown in the last section.

To see the robustness of the topological band gap against the variations of the material parameters, we show the calculated band gap as a function of both γ and $\epsilon_{zz}/\epsilon_{xx}$ in Fig. 9. Clearly the band gap is significant (>0.5) in a wide range of the parameters. For example, when $\epsilon_{zz}/\epsilon_{xx}$ is in between -0.1
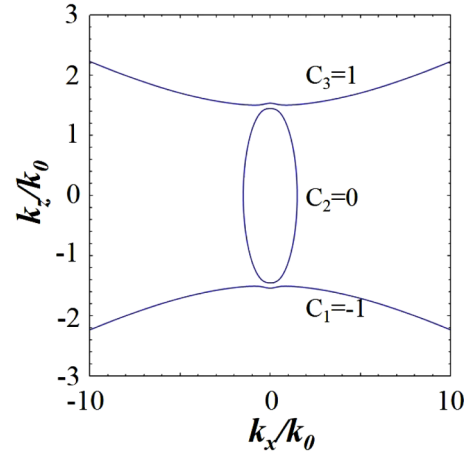

FIG. 8. Calculated EFS of the bilayer superlattice shown in Fig. 7 made of a YIG slab as the gyromagnetic medium and an InSb layer as the metal slab.

and -1.0, the band gap is significant for γ being from 0.4 to 2.0. Interestingly, Fig. 9 shows that for $\epsilon_{zz}/\epsilon_{xx}$ is in between -1.0 and -2.0, one tunes the system from the gapless to the Chern insulating state and then back to gapless state. Finally, it should be pointed out that the present photonic Chern insulator would be much simpler to design and fabricate than many other photonic insulators. For example, the chiral hyperbolic photonic topological insulator reported in Ref. [49] is composed of an array of micrometer-scale helical waveguides. The photonic chiral hyperbolic topological insulators proposed in Ref. [29] would be based on an array of hyperbolic coils which serve as chiral resonators. In contrast, as discussed above, the photonic Chern insulators would consist of a simple YIG/InSb bilayer superlattice, and thus would be much easier to fabricate.

VII. DISCUSSION AND CONCLUSIONS

In the QAH effect, vacuum is an insulator for electrons and thus the chiral edge states are localized at the surface of the Chern insulator. In contrast, vacuum to photons is often like a free electron metal and thus light propagation on the unidirectional edge modes would generally suffer from radiation loss.
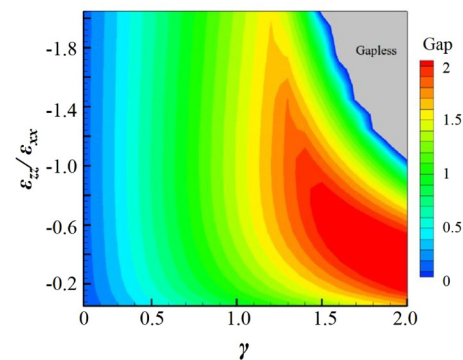

FIG. 9. Calculated band gap map on the $\gamma - (\epsilon_{zz}/\epsilon_{xx})$ plane of the bilayer superlattice shown in Fig. 7, which is made of a YIG slab as the gyromagnetic medium and an InSb layer as the metal slab.
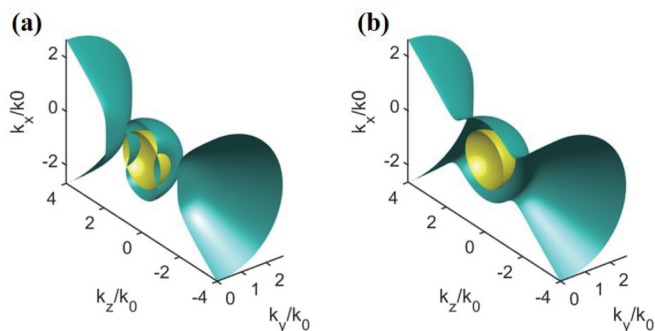
FIG. 10. Bulk EFS (cyan) of lossy GHMs with (a) $\gamma = -1 + 0.1i$ and (b) $\gamma = -1 + 1i$. Here the yellow spheres indicate the EFS of air.
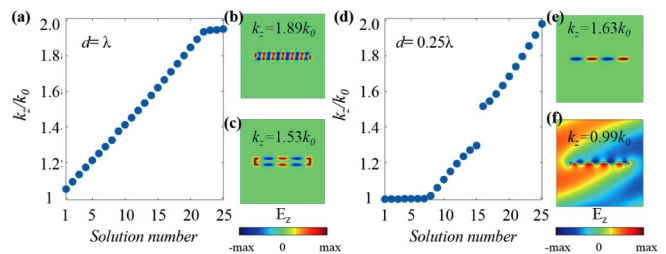

FIG. 11. (a) The eigenmode distribution of a 2D slab of the GHM with $d = \lambda$, (b) the electric field distribution of a bulk mode of $k_z = 1.89k_0$, and (c) the electric field distribution of the edge mode with $k_z = 1.53k_0$. (d) The eigenmode distribution of a 2D slab of the GHM with $d = 0.25\lambda$, (e) the electric field distribution of a bulk mode of $k_z = 1.63k_0$, and (f) the electric field distribution of the edge mode with $k_z = 0.99k_0$.

Consequently, a metal film such as copper is usually inserted between air and the topological photonic insulator to suppress the radiation leakage [22–24]. However, metals like copper could incur significant Ohmic loss. In strong contrast, the chiral edge modes in our GMHs are not only reflection-free but also nonradiative, as demonstrated by our finite element electromagnetic simulations (see Figs. 4 and 5). This is simply because the chiral edge dispersions are located outside light cone [see Fig. 4(b)]. This is an important advantage of the GMHs over the gyromagnetic photonic crystals [22,23].

In conclusion, by both theoretical analysis and electromagnetic simulations, we have demonstrated that gyromagnetic hyperbolic metamaterials (GHM) are photonic Chern insulators with fascinating properties. We further show that the large topological band gaps with a gap Chern number of one in these metamaterials, result from the simultaneous presence of the hyperbolicity and also the gyromagnetic effect, which breaks the time-reversal symmetry and thus gives rise to nonzero Berry curvatures on the EFSs. Remarkably, unlike many other photonic Chern insulators, the GHM Chern insulators possess nonradiative chiral edge modes on their surfaces, and thus allow us to fabricate unidirectional waveguides without cladding metals which generally incur considerable Ohmic loss. Furthermore, the photonic edge states in the proposed Chern insulators are robust against disorder on a wide range of length scales, in strong contrast to crystalline topological insulators, and the light flow direction on the surface of the Chern insulators can be easily flipped by switching the direction of an applied magnetic field. We also uncover a negative refraction of the topological surface wave at the boundary between the GHMs with the opposite signs of gyromagnetic parameters. Finally, we show that compared with other photonic topological materials such as chiral hyperbolic materials [29], the present GHM Chern insulators can be much easier to fabricate.

APPENDIX A: EFFECT OF DISSIPATION

Here we consider two cases with different dissipative losses. In the case of small loss, we set $\gamma = -1 + 0.1i$ in Eq. (2) and also rewrite Eq. (4) as $H\mathbf{E} = 0$. Then the bulk bands are the solutions of eigenequation $\mathrm{Re}[\det(H)] = 0$, as displayed in Fig. 10(a). Clearly the EFS shown in Fig. 10(a) has the same topology as that shown in Fig. 1(d). For the case with large loss, let us set $\gamma = -1 + 1i$ in Eq. (2), and the obtained EFS is plotted in Fig. 10(b). Clearly the EFS now has a distinctly different topology compared with the EFS displayed in Figs. 1(d) and 10(a). In fact, this case belongs to the realm of non-Hermitian optics [50] and thus is beyond the scope of the present paper.

APPENDIX B: FINITE SIZE EFFECT

To examine the finite size effect, we consider a 2D slab of the GHM with varying thickness d. Specifically, we numerically obtain the eigenmodes of the 2D slab with both $d = \lambda$ and $d = 0.25\lambda$ by using COMSOL Multiphysics program, and the main results are displayed in Fig. 11. As shown in Fig. 11(a), the eigenmode distribution is continuous when $d = \lambda$, thereby indicating that there is no significant coupling between the top and bottom edge states and thus the finite size effect can be ignored. The electric field distributions of the bulk mode at $k_z = 1.63k_0$ and the edge mode at $k_z = 1.53k_0$ are displayed in Figs. 11(b) and 11(c), respectively. This supports the statement in Sec. VI that only the modes with $k_z < 1.88k_0$ are the edge modes according to the edge mode dispersion shown in Fig. 4(b). In contrast, Fig. 11(d) shows that there is a forbidden range of k_z when thickness $d = 0.25\lambda$ and smaller, indicating that there exists significant interaction between the top and bottom edge states in this case. Figures 11(e) and 11(f) further display the electric field distributions for the bulk modes with $k_z = 1.63k_0$ and $k_z = 0.99k_0$, respectively. Note that the disappearance of the edge mode here is a finite size effect, as discussed in Ref. [38], rather than a topological effect. Since we focus on only the properties of the bulk and chiral edges of the GHM in this paper, we use the large thickness ($d > \lambda$) of the GHM to avoid the finite size effect.

[1] S. John, Strong Localization of Photons in Certain Disordered Dielectric Superlattices, Phys. Rev. Lett. **58**, 2486 (1987).

[2] E. Yablonovitch, Inhibited Spontaneous Emission in Solid-State Physics and Electronics, Phys. Rev. Lett. **58**, 2059 (1987).

[3] D. R. Smith, J. B. Pendry, and M. C. K. Wiltshire, Science **305**, 788 (2004).

[4] V. G. Veselago, The electrodynamics of substances with simultaneously negative values of ε and μ, Sov. Phys. Usp. **10**, 509 (1968).

[5] H.-C. Chan, S. Sun, and G.-Y. Guo, Near-infrared left-handed metamaterials made of arrays of upright split-ring pairs, J. Phys. D: Appl. Phys. **51**, 265103 (2018).

[6] J. B. Pendry, Negative Refraction Makes a Perfect Lens, Phys. Rev. Lett. **85**, 3966 (2000).

[7] V. Klimov, S. Sun, and G.-Y. Guo, Coherent perfect nanoabsorbers based on negative refraction, Opt. Express **20**, 13071 (2012).

[8] L. Lu, J. D. Joannopoulos, and M. Soljačić, Topological photonics, Nat. Photon. **8**, 821 (2014).

[9] M. Z. Hasan and C. L. Kane, Colloquium: Topological insulators, Rev. Mod. Phys. **82**, 3045 (2010).

[10] X.-L. Qi and S.-C. Zhang, Topological insulators and superconductors, Rev. Mod. Phys. **83**, 1057 (2011).

[11] H. Weng, R. Yu, X. Hu, X. Dai, and Z. Fang, Quantum anomalous Hall effect and related topological electronic states, Adv. Phys. **3**, 227 (2015).

[12] F. D. M. Haldane, Model for a Quantum Hall Effect without Landau Levels: Condensed-Matter Realization of the "Parity Anomaly", Phys. Rev. Lett. **61**, 2015 (1988).

[13] C.-Z. Chang, J. Zhang, X. Feng, J. Shen, Z. Zhang, M. Guo, K. Li, Y. Ou, P. Wei, L.-L. Wang, Z.-Q. Ji, Y. Feng, S. Ji, X. Chen, J. Jia, X. Dai, Z. Fang, S.-C. Zhang, K. He, Y. Wang, L. Lu, X.-C. Ma, and Q.-K. Xue, Experimental observation of the quantum anomalous Hall effect in a magnetic topological insulator, Science **340**, 167 (2013).

[14] F. D. M. Haldane and S. Raghu, Possible Realization of Directional Optical Waveguides in Photonic Crystals with Broken Time-Reversal Symmetry, Phys. Rev. Lett. **100**, 013904 (2008).

[15] Z. Wang, Y. D. Chong, J. D. Joannopoulos, and M. Soljačić, Reflection-Free One-Way Edge Modes in a Gyromagnetic Photonic Crystal, Phys. Rev. Lett. **100**, 013905 (2008).

[16] T. Ochiai and M. Onoda, Photonic analog of graphene model and its extension: Dirac cone, symmetry, and edge states, Phys. Rev. B **80**, 155103 (2009).

[17] Y. Poo, R. X. Wu, Z. Lin, Y. Yang, and C. T. Chan, Experimental Realization of Self-Guiding Unidirectional Electromagnetic Edge States, Phys. Rev. Lett. **106**, 093903 (2011).

[18] W. Tan, L. Chen, X. Ji, and H. Q. Lin, Photonic simulation of topological superconductor edge state and zero-energy mode at a vortex, Sci. Rep. **4**, 7381 (2014).

[19] S. A. Skirlo, L. Lu, and M. Soljačić, Multimode One-Way Waveguides of Large Chern Numbers, Phys. Rev. Lett. **113**, 113904 (2014).

[20] W. He and C. T. Chan, The emergence of Dirac points in photonic crystals with mirror symmetry, Sci. Rep. **5**, 8186 (2015).

[21] H.-C. Chan and G.-Y. Guo, Tuning topological phase transitions in hexagonal photonic lattices made of triangular rods, Phys. Rev. B **97**, 045422 (2018).

[22] Z. Wang, Y. Chong, J. D. Joannopoulos, and M. Soljačić, Observation of unidirectional backscattering-immune topological electromagnetic states, Nature (London) **461**, 772 (2009).

[23] Y. Yang, Y. Poo, R. X. Wu, Y. Gu, and P. Chen, Experimental demonstration of one-way slow wave in waveguide involving gyromagnetic photonic crystals, Appl. Phys. Lett. **102**, 231113 (2013).

[24] S. A. Skirlo, L. Lu, Y. Igarashi, Q. Yan, J. Joannopoulos, and M. Soljačić, Experimental Observation of Large Chern Numbers in Photonic Crystals, Phys. Rev. Lett. **115**, 253901 (2015).

[25] C. He, X.-C. Sun, X.-P. Liu, M.-H. Lu, Y. Chen, L. Feng, and Y.-F. Chen, Photonic topological insulator with broken time-reversal symmetry, Proc. Natl. Acad. Sci. **113**, 4924 (2016).

[26] A. B. Khanikaev, S. Hossein Mousavi, W.-K. Tse, M. Kargarian, A. H. MacDonald, and G. Shvets, Photonic topological insulators, Nat. Mater. **12**, 233 (2013).

[27] T. Ma, A. B. Khanikaev, S. H. Mousavi, and G. Shvets, Guiding Electromagnetic Waves around Sharp Corners: Topologically Protected Photonic Transport in Metawaveguides, Phys. Rev. Lett. **114**, 127401 (2015).

[28] X. Cheng, C. Jouvaud, X. Ni, S. H. Mousavi, A. Z. Genack, and A. B. Khanikaev, Robust reconfigurable electromagnetic pathways within a photonic topological insulator, Nat. Mater. **15**, 542 (2016).

[29] W. Gao, M. Lawrence, B. Yang, F. Liu, F. Fang, B. Beri, J. Li, and S. Zhang, Topological Photonic Phase in Chiral Hyperbolic Metamaterials, Phys. Rev. Lett. **114**, 037402 (2015).

[30] A. Poddubny, I. Iorsh, P. Belov, and Y. Kivshar, Hyperbolic metamaterials, Nat. Photon. **7**, 948 (2013).

[31] M. G. Silveirinha, Chern invariants for continuous media, Phys. Rev. B **92**, 125153 (2015).

[32] V. I. Fesenko and V. R. Tuz, Lossless and loss-induced topological transitions of isofrequency surfaces in a biaxial gyroelectromagnetic medium, Phys. Rev. B **99**, 094404 (2019).

[33] W. Gao, B. Yang, M. Lawrence, F. Fang, B. Beri, and S. Zhang, Photonic Weyl degeneracies in magnetized plasma, Nat. Commun. **7**, 12435 (2016).

[34] D. Wang, B. Yang, W. Gao, H. Jia, Q. Yang, X. Chen, M. Wei, C. Liu, M. Navarro-Cia, J. Han, W. Zhang, and S. Zhang, Photonic Weyl points due to broken time-reversal symmetry in magnetized semiconductor, Nat. Phys. **15**, 1150 (2019).

[35] J. D. Jackson, *Classical Electrodynamics*, 3rd ed. (Wiley, New York, 1999).

[36] T. Fukui, Y. Hatsugai, and H. Suzuki, Chern numbers in discretized Brillouin zone: Efficient method of computing (spin) Hall conductances, J. Phys. Soc. Jpn. **74**, 1674 (2005).

[37] M. I. D'yakonov, New type of electromagnetic wave propagating at the interface, Sov. Phys. JETP **67**, 714 (1988).

[38] V. V. Klimov, D. V. Guzatov, I. V. Zabkov, H.-C. Chan, and G.-Y. Guo, Size and host-medium effects on topologically protected surface states in bianisotropic three-dimensional optical waveguides, Phys. Rev. B **98**, 075433 (2018).

[39] X. Wang, Z. Li, and C.-T. Chan, One-way edge mode in a magneto-optical honeycomb photonic crystal, Phys. Rev. B **80**, 033105 (2009).

[40] H.-X. Wang, Y. Chen, Z. H. Hang, H.-Y. Kee, and J.-H. Jiang, Type-II Dirac photons, npj Quantum Mater. **2**, 54 (2017).

[41] D. Guzatov, V. Klimov, H.-C. Chan, and G.-Y. Guo, Tunning spontaneous radiation of chiral molecules by asymmetric chiral nanoparticles, Opt. Express **25**, 6036 (2017).

[42] H. He, C. Qiu, L. Ye, X. Cai, X. Fan, M. Ke, F. Zhang, and Z. Liu, Topological negative refraction of surface acoustic waves in a Weyl phononic crystal, Nature (London) **560**, 61 (2018).

[43] N. Fang, H. Lee, C. Sun, and X. Zhang, Sub-diffraction-limited optical imaging with a silver superlens, Science **308**, 534 (2005).

[44] Z. Liu, H. Lee, Y. Xiong, C. Sun, and X. Zhang, Far-field optical hyperlens magnifying sub-diffraction-limited objects, Science **315**, 1686 (2007).

[45] I. I. Smolyaninov, Y.-J. Hung, and C. C. Davis, Magnifying superlens in the visible frequency range, Science **315**, 1699 (2007).

[46] K.-M. Lin and G. Y. Guo, Uncoupled modes and all-angle negative refraction in walled honeycomb photonic crystals, J. Opt. Soc. Am. B **25**, C75 (2008).

[47] V. R. Tuz, I. V. Fedorin, and V. I. Fesenko, Bi-hyperbolic isofrequency surface in a magnetic-semiconductor superlattice, Opt. Lett. **42**, 4561 (2017).

[48] H. H. Wu and Y. C. Lan, Magnetic lenses of surface magnetoplasmons in semiconductor-glass waveguide arrays, Appl. Phys. Exp. **7**, 032203 (2014).

[49] M. C. Rechtsman, J. M. Zeuner, Y. Plotnik, Y. Lumer, D. Podolsky, F. Dreisow, S. Nolte, M. Segev, and A. Szameit, Photonic Floquet topological insulators, Nature (London) **496**, 196 (2013).

[50] E. J. Bergholtz, J. C. Budich, and F. K. Kunst, Exceptional topology of non-Hermitian systems, arXiv:1912.10048.